Supplementary Material: Characteristics of Air Entrainment during Dynamic Wetting Failure along a Planar Substrate

E. Vandre [1], M. S. Carvalho [2], and S. Kumar [1]

[1] Department of Chemical Engineering and Materials Science, University of Minnesota, Minneapolis, MN, 55455 USA

[2] Department of Mechanical Engineering, Pontificia Universidade Catòlica do Rio de Janeiro, Rio de Janeiro, RJ, Brazil

This document examines some of the experimental observations that are mentioned, but not fully developed, with the primary article ("Characteristics of Air Entrainment during Dynamic Wetting Failure along a Planar Substrate"). In addition, results are presented from a hydrodynamic model that we have developed in prior work (Vandre *et al.*, 2012, 2013). These numerical results support our comparison of experimental data and model predictions in Section 5 of the primary article.

Figure 1 provides a schematic of the experimental apparatus used for our study of air entrainment. In essence, a substrate is drawn through a glycerol/water bath with increasing speed U, until the onset of air entrainment is visualized at some critical speed U^{crit}. The apparatus allows for control of the liquid viscosity μ_{liq}, the confinement gap H, and the pressure P_{app} applied to the liquid reservoir (see Figure 1a). In addition, the confined meniscus can be located within a parallel channel, as shown in Figure 1b, or positioned against the corner illustrated in Figure 1c, effectively "pinning" the meniscus to a fixed position. (See Section 2 of the primary article for a more detailed description of the apparatus.) Each of these parameters influences the onset of air entrainment, including the critical speed and the shape of entrained air films, as discussed in the following sections.

In Section 1, critical speeds associated with the onset of air entrainment are measured for various liquid viscosities in an unconfined geometry. Section 2 presents fits of an empirical power-law that describes the variation of critical speed with liquid viscosity for different confined geometries. Section 3 describes the relationship between the applied liquid pressure
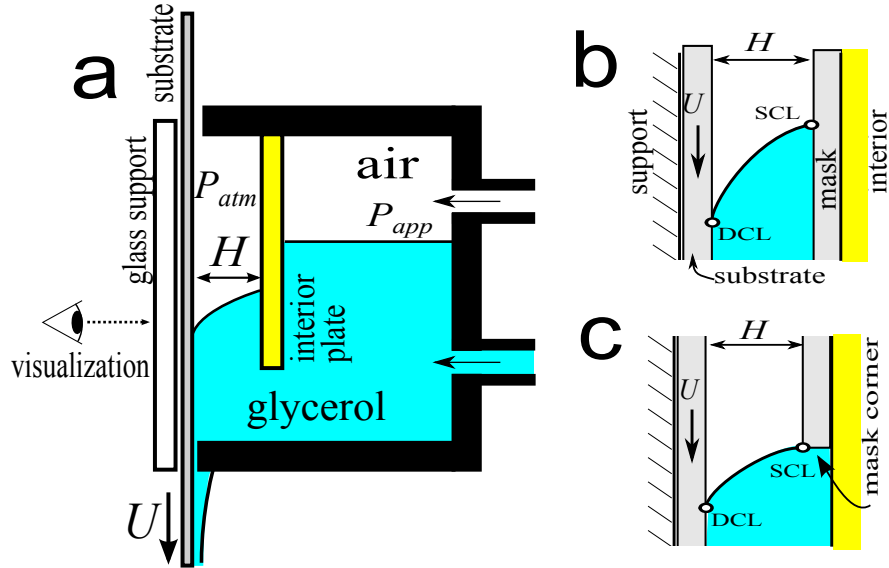
Figure 1: Schematic of the experimental apparatus. (a) Side view of the wetting box. (b) Confinement of the air/liquid interface within a gap H. (c) Confinement with the meniscus effectively pinned on the mask corner.

and the confined meniscus position. In Section 4, visualizations show the effect of substrate speed (Section 4.1) and liquid pressurization (Section 4.2) on the dynamic contact line shape during wetting failure. Section 4.3 discusses the image analysis techniques used to characterize the dimensions of entrained air films. Section 4.4 discusses liquid rewetting sites that nucleate and grow through elongated air films. Lastly, Section 5 evaluates the effects of liquid pressurization using a hydrodynamic model for dynamic wetting and comparisons are made with experimental observations.

1 Liquid Viscosity

Critical speeds systematically decrease with higher liquid viscosities, similar to the findings of prior experimental works (Kistler, 1993; Gutoff & Kendrick, 1982). Figure 2a plots the value of U^{crit} recorded for various glycerol viscosities ($\mu \in [25 \text{ cP } 1000 \text{ cP}]$) using the unconfined geometry ($H \to \infty$). The inverse relationship between critical speed and liquid viscosity (see inset of Figure 2a) suggests that the important parameter is the capillary number $Ca = \mu U / \sigma$, which measures the relative strength of viscous and surface-tension forces
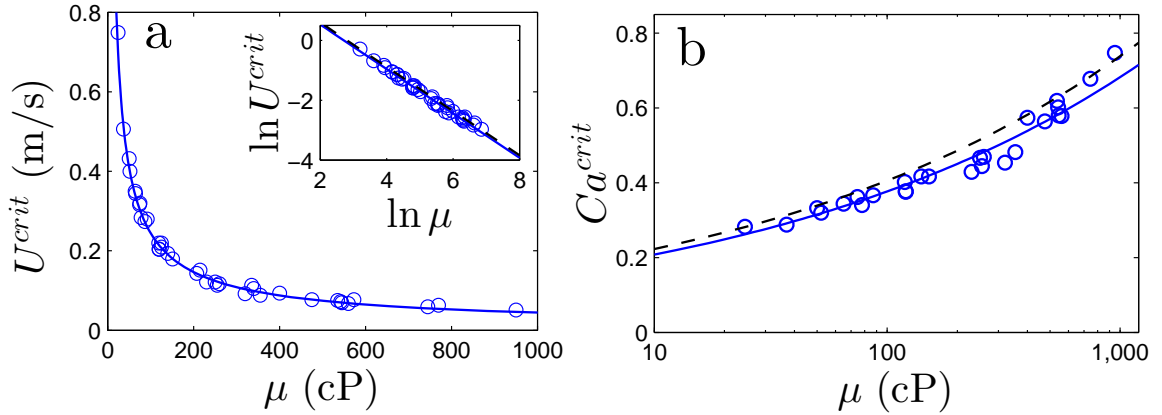
2

Figure 2: (a) Critical speeds measured as a function of glycerol viscosity in the unconfined geometry ($H \to \infty$). The inset demonstrates that critical speed data follow the weak-power law $U^{crit} \propto \mu^{-0.742}$ with the bold line denoting the best fit. (b) Critical capillary numbers corresponding to the data plotted in panel a. The fit from panel a (bold line) is rescaled with μ to match the definition of Ca^{crit}, as expressed by (1) with $K = 0.115$ cP$^{-0.258}$. The dashed line represents the correlation $Ca^{crit} = 0.123[\mu \text{ (cP)}]^{0.26}$, which is obtained from a collection of air-entrainment studies with unconfined geometries (Kistler, 1993).

.

acting on the meniscus.

Figure 2b plots Ca^{crit} values corresponding to the critical-speed data in Figure 2a. Unlike U^{crit}, the critical capillary number increases with higher liquid viscosities, following the weak power-law relationship

$$Ca^{crit} \approx K\mu^{0.258}, \tag{1}$$

where the coefficient K depends on the value of H, as discussed in Section 2. The fit of (1) to the data closely resembles empirical correlations from similar studies of air entrainment in unconfined geometries (Kistler, 1993) (e.g., see dashed line in Figure 2b). Critical capillary numbers Ca^{crit} associated with the onset of air entrainment closely match correlations from previous data sets, which validates the novel experimental apparatus used in this investigation.
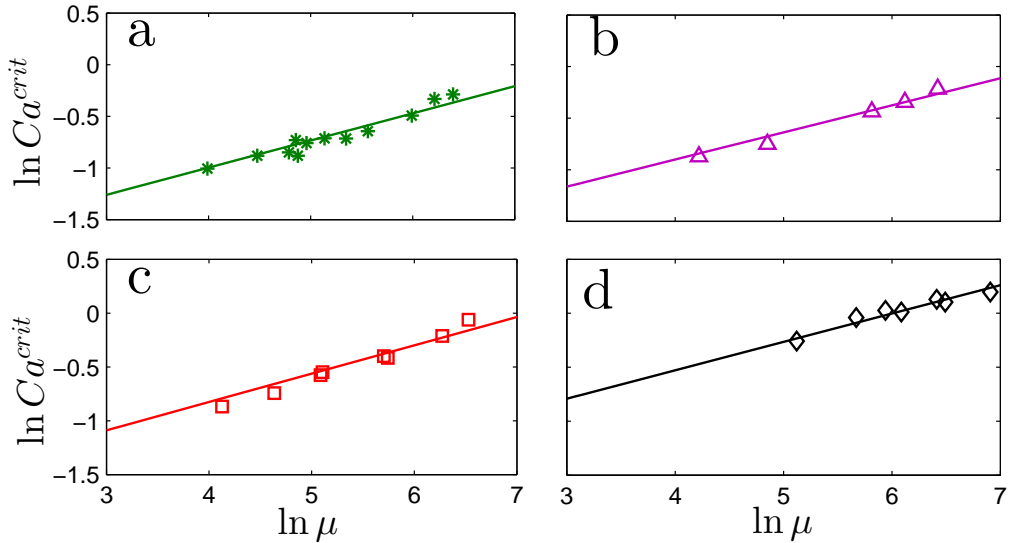
Figure 3: Fits of Ca^{crit} to equation (1) for H = (a) 500, (b) 300, (c) 200, and (d) 100 μm. Fitted values of K = (a) 0.132, (b) 0.146, (c) 0.157, and (d) 0.212 cP$^{-0.258}$.

2 Confinement Fits

Although critical speeds depend on the liquid viscosity, the relative effect of confinement is nearly independent of μ. As a demonstration, Figure 3 plots data sets for each value of H with corresponding fits of (1). For each case, Ca^{crit} data show roughly the same power-law dependence on μ, but shift due to changes to the fitted coefficient K at different values of H.

3 Liquid Pressurization

Liquid pressurization positions the meniscus within the confinement gap during dynamic wetting. Higher applied pressures P_{app} are needed as speed increases in order to resist substrate drag on the meniscus. In fact, the data plotted in Figure 4 suggest that P_{app} must increase linearly with Ca to hold the meniscus position steady within the gap. At fixed Ca, P_{app} is weakly effected by changes to the liquid viscosity (see Figure 4a). In contrast, changes to the gap have a major impact on the required liquid pressure. Since the pressure gradient in channel flow is inversely dependent on the square of the channel height, the applied pressure
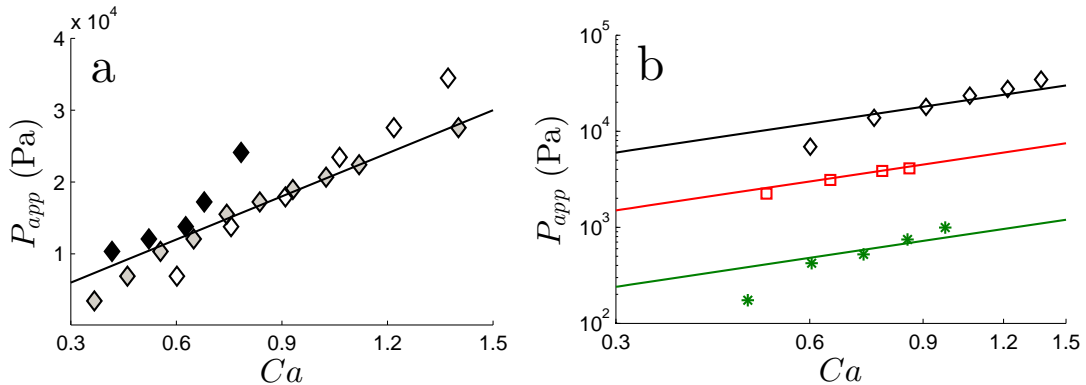
Figure 4: Applied pressure needed to hold meniscus position constant within the confinement gap while increasing Ca. (a) Data are plotted for $\mu = 1000$ cP (white), 600 cP (gray), and 170 cP (black) with $H = 100\mu$m. The solid line represents a linear fit of the $\mu = 500$ cP data. (b) Data are plotted for $H = 100$ μm (diamond), 200 μm (square), and 500 μm (asterisk) with $\mu = 600$ cP. For each data set, the linear fit from panel a is multiplied by the factor $(100 \ \mu\text{m}/H)^2$ to account for the influence of gap width on P_{app}.

must increase with smaller gaps as $P_{app} \propto H^{-2}$ (see Figure 4b). The wetting box becomes susceptible to liquid and compressed-air leaks when $P_{app} > 10^4$ Pa. For this reason, high-speed wetting in gaps less than 100 μm could not be investigated in this study. Furthermore, only high-viscosity solutions ($\mu > 100$ cP) are used with the smallest gap ($H = 100$ μm) to limit the rate of liquid loss.

4 Air-film Shapes

4.1 Low Viscosity

System parameters strongly influence air-film size at the onset of air entrainment. With low-viscosity solutions ($\mu < 40$ cP), a single air film extends across the width of the substrate, pinning on the edges of the tape. In this case W is fixed by the substrate width ($W \approx 5$ cm), making the triangular shape completely specified by the angle ψ. Figure 5 shows that the pinned air film elongates (see Figure 5a-b) as substrate speed exceeds U^{crit}, resulting in larger values of ψ as predicted by theory (Blake & Ruschak, 1979):
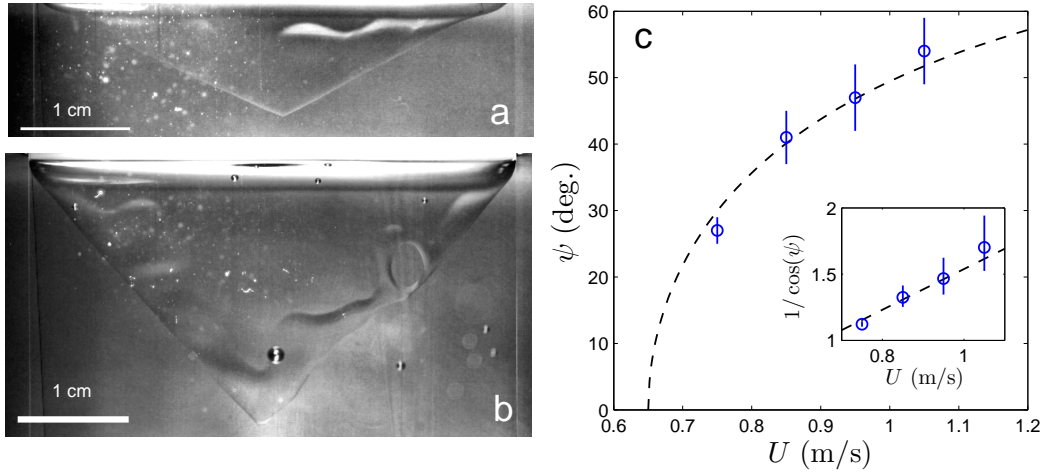
$$\cos \psi = U^{max}/U. \tag{2}$$

Figure 5: The effect of substrate speed on the air-film shape for $\mu = 25$ cP, where a single film spans the width of the substrate at super-critical speeds. The images show the elongation of the air film as speed increases from (a) $U \approx U^{crit}$ (0.75 m/s) to (b) $U > U^{crit}$ (1.05 m/s). (c) The angle ψ is measured as a function of U. *Inset*: The data plotted against the relationship (2). Dashed lines represent (2) using $U^{max} = 0.65$ m/s.

Equation (2) requires that the DCL slope (ψ) increase to maintain a maximum velocity (U^{max}) normal to the DCL as the substrate moves at higher speeds ($U > U^{max}$). Figure 5c demonstrates that (2) matches experimental measurements for ψ as a function of U, although the fitted value of U^{max} underpredicts U^{crit} (measured at the onset of air-film growth) by approximately 10%, similar to the observations of Blake & Ruschak (1979) (Blake & Ruschak, 1979).

4.2 Pressurization

As illustrated in Figure 6, air entrainment is characterized by triangular air films when the meniscus is positioned near the mask corner. Although the meniscus is confined, the SCL remains fixed at the corner, preventing the formation of the broad air film discussed previously. Liquid pressurization tends to decrease the scale of air films that form at the onset of air entrainment. Since narrow gaps allow higher values of P_{app} before depinning the SCL (similar to observations of pressurized fiber coating (Ravinutala & Polymeropoulos, 2002)), much smaller air films are observed with $H = 100$ μm (Figure 6c) than in the other geometries reported in this study (e.g., Figure 6a-b).
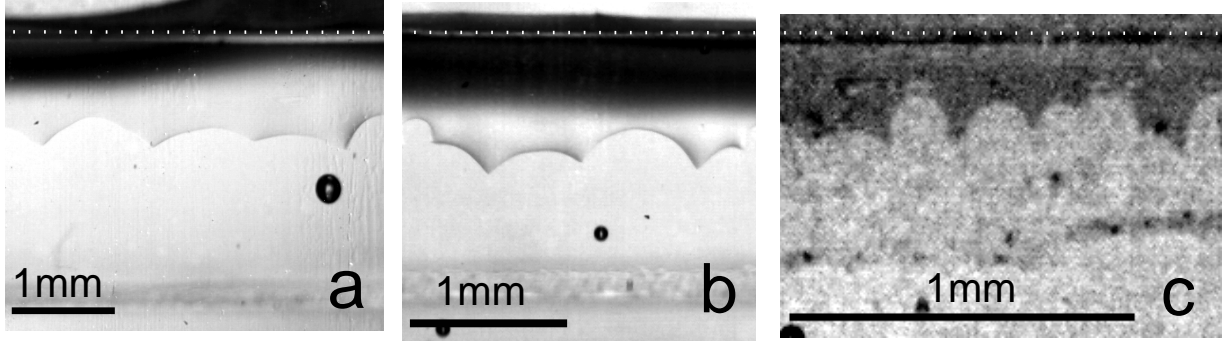
6

Figure 6: Visualization of DCL shapes at the onset of air entrainment for confined systems: (a) $\mu = 515$ cP, $H = 500\mu$m, and $P_{app} = 1.3$ kPa; (b) $\mu = 460$ cP, $H = 200\mu$m, and $P_{app} = 6.9$ kPa; (c) $\mu = 600$ cP, $H = 100\mu$m, and $P_{app} = 27.5$ kPa;. In each case, the meniscus is positioned near the mask corner (white dotted line), allowing pressurization to reduce the size of air films relative to the unconfined system. Scale bars denote lengths of 1 mm for each figure.

4.3 Air-film Measurements

Visualizations are analyzed with software from the MATLAB Image Processing Toolbox$^{\text{TM}}$ in order to measure the dimensions of entrained air films. First, recorded images are converted to greyscale and contrast is enhanced using the *imadjust* function in MATLAB$^{\circledR}$. Figure 7a demonstrates that this contrast filter is typically sufficient to clearly expose the triangular air films that form at the onset of air entrainment (i.e., Ca^{crit}). Second, an edge-detection algorithm (the *edge* function with the "Canny" method) is used to segment the image, as shown in Figure 7b. Lastly, the pixels bounding a single triangular air film (i.e., the dynamic contact line) are used to fit two distinct lines that intersect near the vertex of the air film. These linear fits are used to define the two equal sides of an isosceles triangle. The base of the isosceles triangle is positioned at the point where the fitted triangle width deviates by approximately 25% from the width of the true air-film shape. As shown by Figure 7, this procedure does a fairly good job of capturing the air-film shape and provides a reproducible method for measuring the width W and angle ψ associated with the triangular air films.

Using the procedure above, at least six distinct air films were analyzed to obtain statistical samples of W for each glycerol/water solution that was visualized during this study. Figure
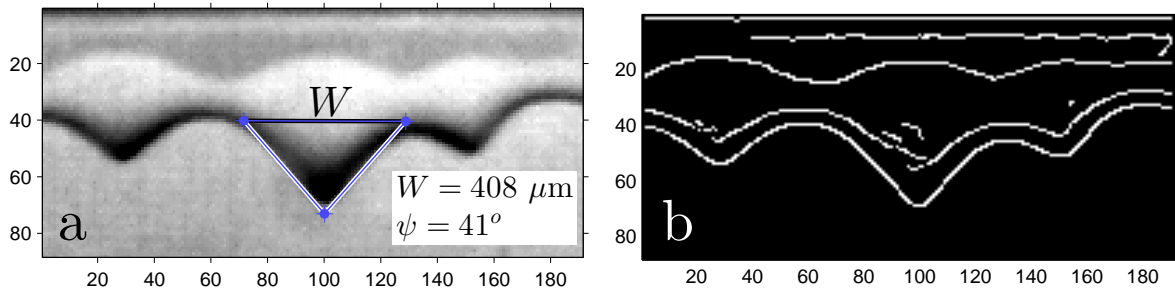
7

Figure 7: Measurement of air-film width for $\mu = 1000$ cP at Ca^{crit} in the unconfined geometry ($H \to \infty$). (a) The greyscale visualization image (contrast filter applied) with an isosceles triangle of base width W and angle ψ fit to the triangular air film. (b) Rendered image of the air film using the edge-detection method described in text. In each visualization image, 140 pixels (number on axes) corresponds with a distance of approximately 1 mm.
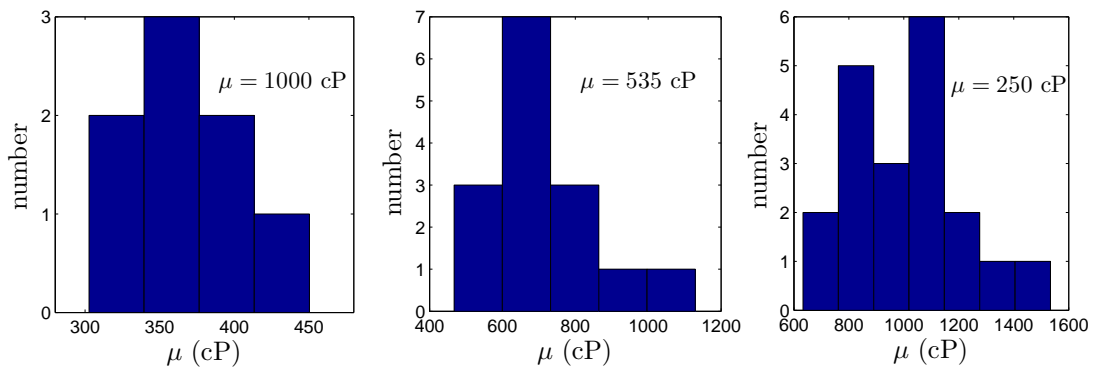

Figure 8: The distribution of air-film widths W for different liquid viscosities (μ values listed in each panel) measured at Ca^{crit} in the unconfined geometry ($H \to \infty$). Refer to Figure 7 for the measurement technique.

8 plots the distribution of air-film widths measured for three different values of μ. Each data set resembles a normal distribution with a standard deviation of less than 25%, which seems to be a reasonable uncertainty considering the somewhat crude measurement method.

Image processing is also used to estimate the thickness h_f of air films. In this case, a sequence of frames is analyzed to capture air-film rupture, which releases a discrete film of air that rapidly evolves into a spherical bubble. (See Section 4.3 of the primary article for further discussion of this event.) The mean air-film thickness h_f is approximated by
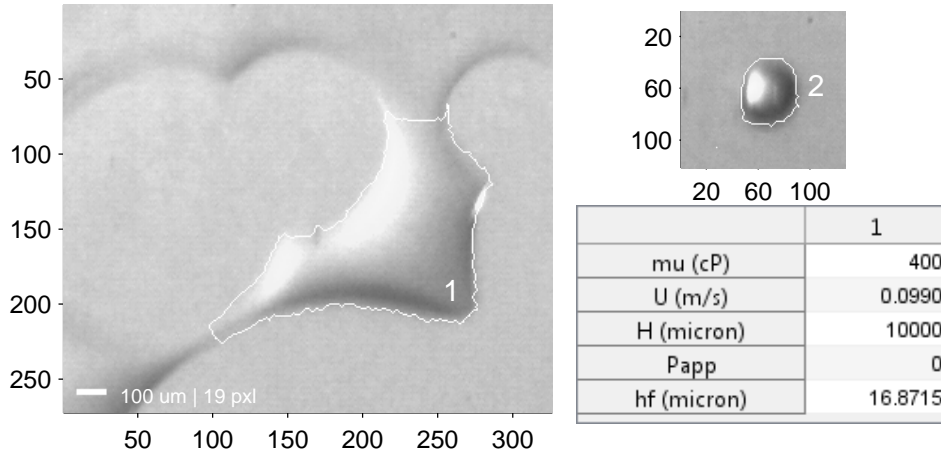
$$h_f = \frac{\pi D^3}{6A} \tag{3}$$

8

Figure 9: Measurements associated with the calculation of air-film thickness h_f for $\mu = 400$ cP at Ca^{crit} in the unconfined geometry ($H \to \infty$). In each image, 190 pixels (values on axes) corresponds to approximately 1 mm.

where A is the area of the ruptured air film and D is the resulting bubble diameter.

Image segmentation is achieved using the contrast filters and edge-detection algorithms discussed above. Following this procedure, regions associated with the air domain can be isolated in order to measure A and D in the case of the film and bubble, respectively. Figures 9 and 10 demonstrate this procedure, where region "1" denotes the initial air-film area and region "2" marks the resulting air bubble. The air-film height h_f is calculated by substituting the measurements for A and D into (3).

Unfortunately, this measurement is fairly sensitive to the time (i.e., the frame) at which the air-film area is analyzed. This is because the air film only remains relatively flat and two-dimensional at early times in the rupture process (Figure 9). As rupture proceeds, capillary forces cause the air pocket to become more compact and curved (Figure 10), resulting in higher mean thickness than would be present in the original air film. For example, h_f values differ by approximately a factor of two when comparing the images in Figures 9 and 10 (the frames separated by approximately 1 ms). Values of h_f reported in the primary article correspond to measurements made early in the rupture sequence (similar to Figure 9) since the air film remains nearly flat during these times. The increase in h_f at later times is accounted for in the reported uncertainty.
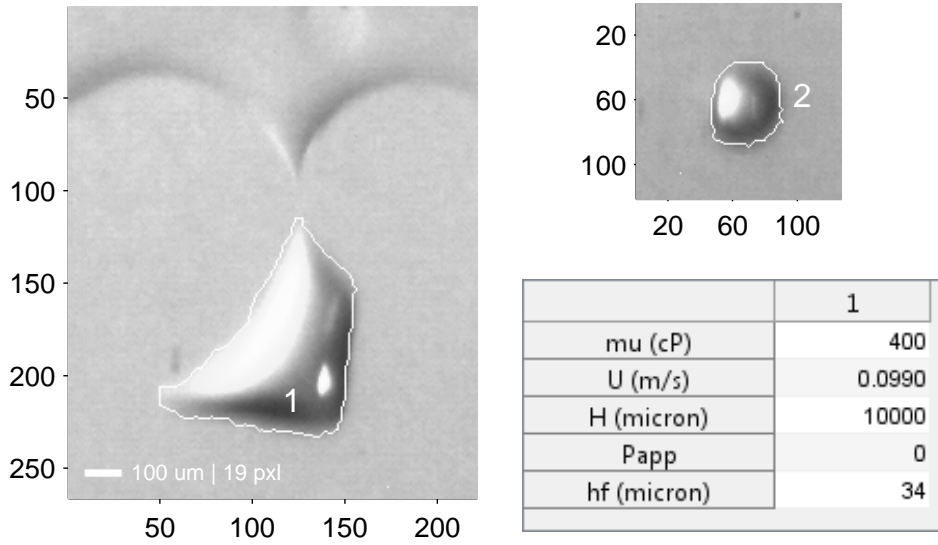
	1
mu (cP)	400
U (m/s)	0.0990
H (micron)	10000
Papp	0
hf (micron)	34

Figure 10: The same procedure as shown above, only the air film is analyzed at approximately 1 ms later than the image in Figure 9.

4.4   Rewetting Sites

Rupture is initiated by a point of liquid-substrate contact that pierces through the air film. Once nucleated, the liquid rewetting sites grow rapidly. The panels of Figure 11 compare the shapes of the rewetting sites at Ca^{crit} for air/glycerol solutions of $\mu = 25$ cP (Figure 11a-b) and $\mu = 400$ cP (Figure 11c-d). In both cases, rewetting begins with a circular region of liquid contact that becomes slightly oblong because the sites grow most quickly in the direction of substrate motion. In fact, the speed of the rewetting rim tends to exceed the substrate speed, as shown by the data in Figure 11e. This suggests that in addition to substrate drag, liquid is driven toward the rewetting surface by effects of the wetting dynamics or local flow field, allowing the rewetting rim to advance faster than the substrate. Further investigation is required to better understand the dynamics of this rewetting behavior.
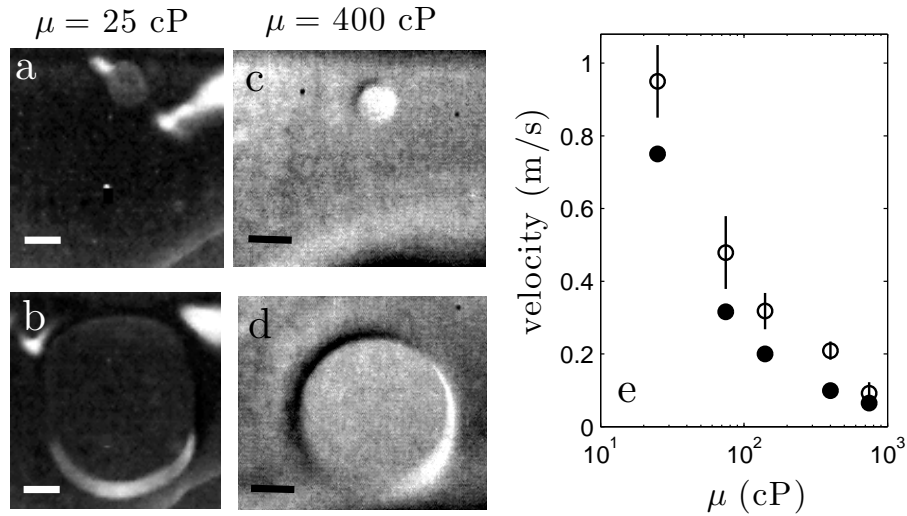
10

Figure 11: The growth of rewetting sites in elongated air films. Images are shown for (a-b) $\mu = 25$ cP and (c-d) $\mu = 400$ cP at Ca^{crit}. Top and bottom frames are separated by a time of 4 ms for both fluids. Scale bars in lower left corners mark lengths of (a-b) 1 mm and (c-d) 0.25 mm. (e) Comparison of substrate speed (closed symbols) and downward velocity of rewetting rims (open symbols) at Ca^{crit} for variety glycerol/water solutions.

5 Hydrodynamic Model

This section explores the effect of liquid pressurization using a hydrodynamic model for dynamic wetting that we have developed in a prior work (Vandre *et al.*, 2012). A single geometry is considered in which the air/liquid meniscus is confined to a gap $H = 100$ μm in a parallel channel. Since this simplified geometry does not include the mask corner used to experimentally pin the meniscus (refer to Figure 1), pressurization is controlled with imposed pressure gradients that are similar in form to a body force acting on the liquid. Model predictions are compared against experimental data for an equivalent gap with liquid viscosity $\mu = 600$ cP.

The two-dimensional model system is illustrated in Figure 12, where an impenetrable air/liquid interface with surface tension σ resides within a gap H between a stationary plate (top) and a substrate (bottom) that moves at speed U. Since we consider a confined interface ($H = 100$ μm), inertial effects are neglected, resulting in the creeping-flow equations for the
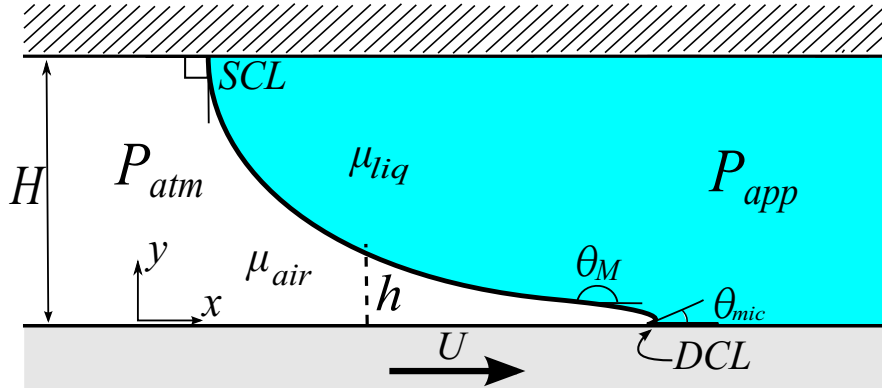
11

Figure 12: Schematic of the hydrodynamic model.

fluid velocities $\boldsymbol{v}$ and pressures p:

$$\boldsymbol{\nabla} \cdot \boldsymbol{v} = 0, \quad \boldsymbol{\nabla} p = \mu \nabla^2 \boldsymbol{v}, \tag{4}$$

where the fluid viscosity μ adopts values μ_{liq} and μ_{air} for the liquid and air, respectively.

Standard normal-stress, tangential-stress, and kinematic conditions are imposed at the fluid interface $y = h$. Velocity and interface angle conditions are prescribed at the static contact line (SCL) and the dynamic contact line (DCL). For simplicity, microscopic contact angles are fixed to $\theta_{mic} = 90^o$ at both the SCL and the DCL. The no-slip condition ($\boldsymbol{v} = 0$) is assumed at the stationary plate, whereas a Navier-slip condition is applied along the substrate with slip length $l_{slip} = 100$ nm. The governing equations are solved with the Galerkin finite element method (FEM) with elliptic mesh generation (Christodoulou & Scriven, 1992). A more complete description of the governing equations and numerical technique can be found in our prior work (Vandre et al., 2012, 2013; Vandre, 2013).

Solutions to the model discussed above describe steady-state wetting in a parallel channel, similar to the confinement system used experimentally (refer to Figure 1b). As discussed in Section 3, substrate drag is balanced by pressure P_{app} applied to the liquid flow downstream from the meniscus. The applied pressure P_{app} can be used to adjust the meniscus position along the substrate, but does not affect the interface shape or wetting state. In order to hold meniscus position constant, P_{app} must increase nearly linearly with Ca, similar to the

12

experimental data plotted in Figure 4.

Pressurization effects arise from changes to the pressure *gradients* in the liquid flow. Experimentally, pressure gradients can be influenced when the meniscus is pinned against a corner as shown in Figure 1c. Since the corner obstructs meniscus motion, changes to P_{app} affect the liquid flow and interface shape. In order to model pressurization without considering this complicated domain geometry (refer Figure 1c) we modify the x-component of (4) for the liquid:

$$\frac{\partial p}{\partial x} = \mu_{liq}\frac{\partial^2 u}{\partial y^2} + \frac{\Delta P_{app}}{H}. \tag{5}$$

Here, u is the x-component of the liquid velocity and ΔP_{app} represents an increase in the applied liquid pressure ($\Delta P_{app} \geq 0$). Similar to a body force, $\Delta P_{app}/H$ contributes a constant pressure gradient in (5) that augments liquid pressures downstream from the fluid interface. This effectively pressurizes the liquid flow while keeping the meniscus position fixed, similar to that which is achieved with the cornered geometry in the experimental system.

The onset of air entrainment is determined by tracing steady-state solution paths to faster substrate speeds (larger capillary numbers $Ca = \mu_{liq}U/\sigma$) until locating a turning point at a critical capillary number Ca^{crit}. Since two-dimensional steady states cease to exist at higher speeds, Ca^{crit} denotes the transition to unsteady or three-dimensional flow, consistent with our experimental observations of air entrainment. Our prior work contains details about solution paths and flow fields predicted from the hydrodynamic model (Vandre *et al.*, 2013).

Similar to our experimental findings, the model shows that liquid pressurization delays air entrainment to faster substrate speeds. As plotted in Figure 13a, the model predicts that the critical capillary number increases by a percentage ΔCa^{crit} that grows with ΔP_{app}. Direct comparison with experimental data is challenging since we do not model the identical system geometry. Specifically, the value of the applied liquid pressure P_{app} depends on the domain shape and the location of the measurement. (Recall that in the experimental system P_{app} is measured in the liquid reservoir, outside of the confinement channel.) As an approximation, the applied liquid pressure can be computed from the model with the value of a pressure
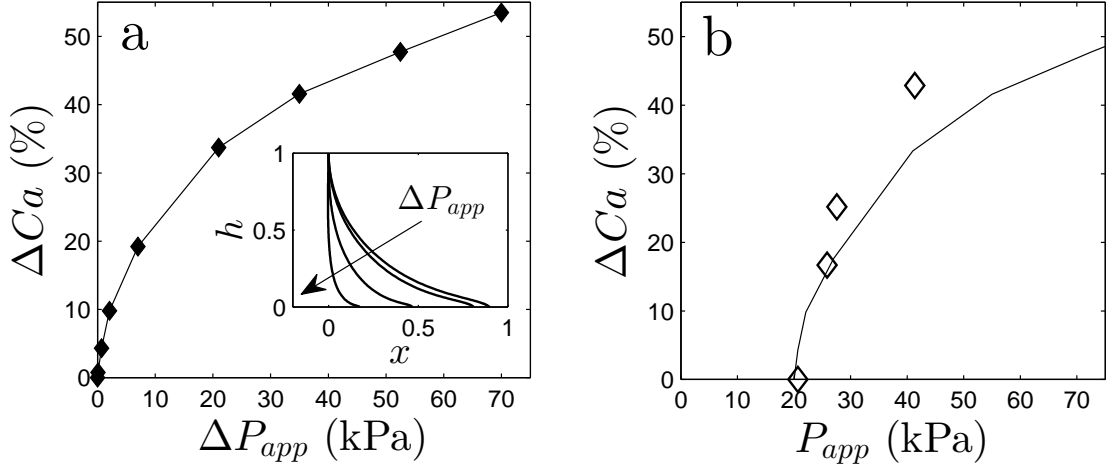
Figure 13: Comparison of pressurization effects from model predictions and experimental measurements. (a) Model predictions for the percent change in the critical speed as a function of ΔP_{app} in (5). *Inset*: Interface profiles at Ca^{crit} for $\Delta P_{app} =$ 0 kPa, 0.7 kPa, 7 kPa, and 70 kPa. (b) Comparison with experimental measurements (open symbols) of the change in critical speed at various P_{app}. Note that the model prediction (line) is simply taken from panel (a) using $P_{app} = \Delta P_{app} + p_0$, where $p_0 \approx 2$ kPa, as described in the text. Parameters for experimental system: $H = 100$ μm, $\mu_{liq} = 600$ cP, $\sigma = 65$ mN/m; model parameters: $H = 100$ μm, $\mu_{liq} = 1$ cP, $\sigma = 70$ mN/m, and $l_{slip} = 100$ nm. (See references Vandre *et al.* (2012) and Vandre *et al.* (2013) for description of the slip length l_{slip} used in the model.)

datum p_0 that is fitted to the experimental data, such that $P_{app} = \Delta P_{app} + p_0$. Figure 13b shows that model predictions qualitatively match the trend of experimental results when $p_0 \approx 2$ kPa. Here, p_0 is selected to match the experimental value of P_{app} needed to position the meniscus at the corner during the first signs of wetting failure (corresponding to $Ca^{crit} \approx 1.12$ and $\Delta Ca^{crit} \approx 0$). Any further increase in P_{app} pressurizes the liquid ($\Delta P_{app} > 0$), leading to higher critical speeds, in agreement with the model predictions.

Furthermore, the hydrodynamic model predicts that liquid pressurization shortens the meniscus, qualitatively matching experimental visualizations (e.g. Figure 6). The inset of Figure 13a illustrates that the interface length decreases by nearly an order of magnitude when ΔP_{app} increases to 70 kPa. This change in scale roughly approximates the effect of pressurization on the size of triangular air films that are experimentally observed at the onset of wetting failure (see Figure 11 in primary article).

References

Blake, T. D. & Ruschak, K. J. 1979 A maximum speed of wetting. *Nature* **282**, 489–491.

Christodoulou, K. N. & Scriven, L. E. 1992 Discretization of free surface flows and other moving boundary problems. *Journal of Computational Physics* **99**, 39–55.

Gutoff, E. B. & Kendrick, C. E. 1982 Dynamic contact angles. *AIChE Journal* **28**, 459–466.

Kistler, S. F. 1993 Hydrodynamics of wetting. In *Wettability* (ed. John C. Berg), pp. 311–429. Marcel Dekker, Inc.

Ravinutala, S. & Polymeropoulos, C. 2002 Entrance meniscus in a pressurized optical fiber coating applicator. *Experimental Thermal and Fluid Science* **26**, 573 – 580.

Vandre, E. 2013 Onset of dynamic wetting failure: The mechanics of high-speed fluid displacement. PhD thesis, University of Minnesota.

Vandre, E., Carvalho, M. S. & Kumar, S. 2012 Delaying the onset of dynamic wetting failure through meniscus confinement. *Journal of Fluid Mechanics* **707**, 496–520.

Vandre, E., Carvalho, M. S. & Kumar, S. 2013 On the mechanism of wetting faluire during fluid displacement along a moving substrate. *Physics of Fluids* **25**, 102103.